UNIVERSIDAD SAN FRANCISCO DE QUITO USFQ

Colegio de Ciencias e Ingeniería

Development of Ab-initio molecular dynamics protocol to simulate the temperature effect in a Graphene–silicon Schottky junction using VASP

Bryan Mauricio Sanango Chicaiza

Física

Trabajo de titulación presentado como requisito

para la obtención del titulo de

Licenciado en Física

September 10, 2024

UNIVERSIDAD SAN FRANCISCO DE QUITO USFQ

Colegio de Ciencias e Ingeniería

HOJA DE CALIFICACIÓN DE TRABAJO DE FIN DE CARRERA

Bryan Mauricio Sanango Chicaiza

Nombre del profesor, Titulo académico: Javier Torres, PhD

September 10, 2024

© Derechos de Autor

Por medio del presente documento certifico que he leído todas las Políticas y Manuales de la Universidad San Francisco de Quito USFQ, incluyendo la Política de Propiedad Intelectual USFQ, y estoy de acuerdo con su contenido, por lo que los derechos de propiedad intelectual del presente trabajo quedan sujetos a lo dispuesto en esas Políticas.

Asimismo, autorizo a la USFQ para que realice la digitalización y publicación de este trabajo en el repositorio virtual, de conformidad a lo dispuesto en la Ley Orgánica de Educación Superior del Ecuador.

Nombres y apellidos:	Bryan Mauricio Sanango Chicaiza
Código:	00209943
Cédula de Identidad:	0302103676
Lugar y fecha:	September 10, 2024

ACLARACIÓN PARA LA PUBLICACIÓN

Nota: El presente trabajo, en su totalidad o cualquiera de sus partes, no debe ser considerado como una publicación, incluso a pesar de estar disponible sin restricciones a través de un repositorio institucional. Esta declaración se alinea con las prácticas y recomendaciones presentadas por el Committee on Publication Ethics COPE descritas por Barbour et al. (2017) Discussion document on best practice for issues around theses publishing, disponible en `http://bit.ly/COPETheses`

UNPUBLISHED DOCUMENT

Note: The following capstone project is available through Universidad San Francisco de Quito USFQ institutional repository. Nonetheless, this project – in whole or in part – should not be considered a publication. This statement follows the recommendations presented by the Committee on Publication Ethics COPE described by Barbour et al. (2017) Discussion document on best practice for issues around theses publishing available on `http://bit.ly/COPETheses`

Agradecimientos

Quiero agradecer a mi familia. Ellos creyeron en mí incluso cuando yo hacía mucho que había dejado de hacerlo. Agradezco el apoyo a lo largo de estos años en los que mi mamá me brindaba consuelo, mi papá me daba coraje y mi hermana me daba una razón para sonreír. Agradezco a las personas que encontré en el camino y que, con paciencia y comprensión, estuvieron ahí para mí en todo momento. Quiero agradecer a aquellos que me acompañaron en los momentos en los que no era, digamos, una persona fácil de acompañar. Quiero agradecer a esas personas que me ayudaron a recordar la belleza de momentos tan simples como tomar un café, comer alitas, jugar al cuarenta, ver una pintura y contemplar un atardecer. Agradezco a todas las personas que estuvieron ahí cuando era y cuando dejé de ser. Esas personas tan especiales que parecen venir del espacio exterior, de un mundo mágico o de un jardín de tulipanes. A esas personas no puedo hacer más que agradecerles. También quiero agradecer al QCT y, en especial, a Javier, quienes me acogieron y tuvieron una paciencia de santo conmigo. Sé que no fue fácil, pero agradezco su compañía, consejo y regaño por igual. Seguro que me falta mucho más por agradecer, pero el tiempo apremia. Y, como un gesto extraño y quizás algo estrambótico, gracias a ti que te tomaste el tiempo de leer este agradecimiento.

Resumen

Esta tesis amplía un estudio previo sobre la unión Schottky de grafeno-silicio (G/S SJ) que relacionó las variaciones geométricas con cambios en sus propiedades electrónicas. Para caracterizar mejor la G/S SJ, este estudio introduce el efecto de la temperatura utilizando el software VASP, planteando la hipótesis de que los cambios en la estructura atómica inducidos por la temperatura impactan su comportamiento electrónico. Se lograron tres objetivos: validar los métodos de VASP 6.4.2 replicando análisis geométricos previos, desarrollar un protocolo de dinámica molecular ab initio para la termalización y evolución de la G/S SJ a 300K, 400K y 500K, y caracterizar las propiedades electrónicas específicas de cada temperatura mediante simulaciones a nivel cuántico-mecánico en QuantumATK y simulaciones a nivel de dispositivo en Sentaurus. Los resultados afirman que la temperatura altera significativamente el comportamiento electrónico de la G/S SJ, apoyando la hipótesis y ampliando la investigación previa.

Palabras clave: *Ab-initio, VASP, Diodo Schottky de Grafeno/Silicio*

Abstract

This thesis expands upon a previous study on the graphene-silicon Schottky junction (G/S SJ) that linked geometric variations to changes in its electronic properties. To better characterize the G/S SJ, this study introduces the effect of temperature using VASP software, hypothesizing that temperature-induced changes in the atomic structure impact its electronic behavior. Three objectives were achieved: validating the methods of VASP 6.4.2 by replicating previous geometric analyses, developing an ab initio molecular dynamics protocol for the thermalization and evolution of the G/S SJ at 300K, 400K, and 500K, and characterizing the electronic properties specific to each temperature using quantum-mechanical simulations in QuantumATK and device-level simulations in Sentaurus. The results affirm that temperature significantly alters the electronic behavior of the G/S SJ, supporting the hypothesis and extending the previous research.

Keywords: *Ab-initio, VASP, Graphene–Silicon Schottky Diode*

Contents

List of Tables

List of Figures

Chapter 1

Introduction

Over the past decade, graphene has become one of the most studied materials due to its exceptional mechanical, optical, and electrical properties, making it an ideal candidate for both investigating fundamental problems in physics and developing innovative nanoelectronic devices [1]. Previous research has demonstrated that graphene can form junctions with both 3D and 2D semiconducting materials, which exhibit rectifying characteristics and function as excellent Schottky diodes [2]. Among these, the graphene–silicon Schottky junction (G/S SJ) is particularly noteworthy, as it has been proposed as an efficient architecture for photodetection [3]. See Fig.1.1. for a graphical representation of the G/S SJ.

Despite the promising applications of the G/S SJ and similar devices, they have only become the subject of systematic investigation within the past decade [2]. The manufacturing and fine-tuning of these junctions for practical applications are hindered by the lack of precise data on their structural and electronic proper-
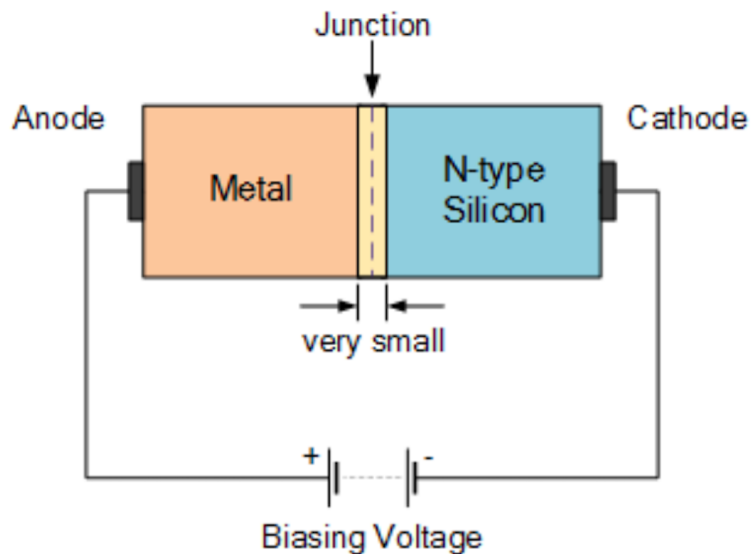
Figure 1.1: Graphical representation of the G/S SJ

ties. The fabrication of graphene–silicon Schottky diodes (G/S SD) through the deposition of mechanically exfoliated graphene onto silicon substrates [4] served as an important starting point. This work yielded several important findings: a Schottky barrier forms at the interface between graphene and silicon in a G/S SD, the magnitude of the photocurrent across the G/S SD is spatially dependent, and the electrical current in these devices is influenced by temperature [4]. However, despite the importance of these conclusions, further research has been limited due to the high costs associated with fabricating G/S SDs [5], [6], [7].

In this context, alternative approaches become desirable, and Computer Modeling and Simulation (CMS) methods emerge as a promising solution. CMS has demonstrated its ability to provide theoretical insights, such as the electronic band structure, vibrational modes, and diffusion mobility of atoms and ions on the sur-

face of graphene [8], [9], [10], [11]. Therefore, CMS is a powerful tool for predicting the properties of graphene-based composites, investigating feasible applications, and providing new ideas and theoretical validation for experimental research [8]. Among CMS methods, Density Functional Theory (DFT) and Molecular Dynamics (MD) have significantly contributed to understanding condensed matter systems [12], [13], [14], [15], [16], [17]. However, both approaches have limitations. DFT is fundamentally a ground-state method [18], typically performed at 0K on systems fixed at their crystallographic positions. On the other hand, MD calculations for practical applications often require empirical interatomic potentials within a defined framework, using parameters and prescribed functional forms to match the system's properties to experimental data [19]. A revolutionary approach by Car and Parrinello bridged these methods, enabling the application of DFT to MD for solving the electronic structure of very large or disordered systems [14]. The resulting method, known as Car-Parrinello Molecular Dynamics (CPMD), laid the foundation for Ab-initio Molecular Dynamics (AIMD) [15]. Subsequent advancements, such as the development of the projector-augmented-wave (PAW) method, have further increased the impact of DFT on materials research [20].

In a study conducted by Paredes & Beltrán [21], a G/S SJ was simulated using quantum-mechanical and electrodynamical analyses. It was found that variations in the geometry of the device—specifically its atomic structure—led to changes in its electrical properties. That investigation was based on the Born-Oppenheimer approximation, which did not account for the effect of temperature on the system. In the present study, we aim to extend this analysis by examining the impact of temperature on the electronic properties of the device. Our hypothesis is that

the relationship between temperature and electronic properties is indirect, with temperature-induced modifications in the atomic structure of the G/S SJ subsequently altering its electronic behavior. To test this hypothesis, for this thesis the following three objectives were established:

1. **Validation of methods in VASP version 6.4.2:** In the study conducted by Paredes & Beltrán, a quantum-mechanical investigation was conducted to analyze the effect of geometry on the electronic properties of the G/S SJ [21]. Specifically, the impact of varying the distance between the graphene sheet and the silicon bulk on the electronic structure was explored. This was done using DFT and plane-wave simulations in Quantum-ATK software to determine the band structure, effective mass, and Fermi level. VASP version 5.4.4 was employed in that analysis. For the present study, we will use version 6.4.2 of VASP, which allows for the incorporation of temperature effects. To validate the methods a similar analysis of the graphene-silicon distance will be performed, and the results will be compared to those from the study conducted by Paredes & Beltrán, to ensure consistency and reliability.

2. **Establish an AIMD protocol:** Input parameters for running AIMD calculations in VASP were tested. The protocol began with an optimized G/S SJ model, which was thermalized using a Nosé–Hoover thermostat. Subsequently, the system was allowed to evolve dynamically without energy exchange. Representative structures of the system were extracted from the final stage of this process. The protocol was applied to the optimized G/S SJ model at three different temperatures: 300K, 400K, and 500K

3. **Characterizing of the G/S SJ:** Each representative structural samplings of the device at a given temperature was exported as a CIF file and analyzed in Quantum-ATK to determine its Fermi level and effective mass. The average Fermi level and effective mass were calculated for the three temperatures. Finally, these averaged values were used in a device level model implemented in Sentaurus software to generate three current-voltage (IV) characteristic curves.

Chapter 2

Theoretical framework

2.1 Introduction to Density Functional Theory

We will give an introduction to Density Functional Theory (DFT), focusing on the basics since our interest in DFT lies in its function as a tool to generate potentials that will be used for Ab-initio molecular dynamics calculations [22].

Any attempt to understand the properties of materials, such as their electrical or magnetic characteristics, requires a thorough comprehension of the behavior of the atoms, electrons, and ions that compose them, as well as their distribution and the system's response to external disturbances [12]. For instance, consider a system of N electrons of mass m_e interacting with a field of M ions of mass M_A, each with its respective charge Z_A. The Hamiltonian of the system is the following:

$$H = -\sum_{i=1}^{N} \frac{\hbar^2}{2m_e} \nabla_i^2 - \sum_{A=1}^{M} \frac{\hbar^2}{2M_A} \nabla_A^2 + \sum_{i<j}^{N} \frac{e^2}{|\mathbf{r}_i - \mathbf{r}_j|} + \sum_{A<B}^{M} \frac{Z_A Z_B e^2}{|\mathbf{R}_A - \mathbf{R}_B|} - \sum_{i=1}^{N} \sum_{A=1}^{M} \frac{Z_A e^2}{|\mathbf{r}_i - \mathbf{R}_A|}$$
$$(2.1)$$

the first two terms correspond to the kinetic energy of the electrons and ions respectively, the third term indicates the potential energy of repulsion between the electrons, the fourth is the potential energy of repulsion between the ions, and the fifth indicates the potential energy of attraction between the electrons and the ions. Solving Eq.2.1 for this system rapidly becomes complex [23].

To facilitate the resolution of this problem, different approximations can be used. One approximation is the Born-Oppenheimer approximation, where the total wave function is written as the product of the electronic wave function with the ionic wave function [12], thus reducing the whole problem to an electronic-only one for fixed ion positions [23].

One may start from the Born-Oppenheimer approximation and ask whether it is possible to obtain useful information from a quantum system without needing to consider explicitly all the electrons [24]. An affirmative answer for the latter resides in the DFT, where early developments involved several models attempting to describe the energy of a system as a functional of the electron density. These early models only loosely described electron density, as they were based on the properties of a uniform electron gas to describe atoms and molecules [25].

In the mid-1960s, Hohenberg, Kohn, and Sham demonstrated that knowledge

of the electron density alone is sufficient to derive relevant quantitative information about any system [24]. Hohenberg and Kohn introduced two foundational theorems of DFT. The first theorem states: *The ground state electron density determines the external potential, within an additive constant* [26]. Thus, for a non-degenerate system, the ground-state density $\rho_0(\mathbf{r})$ determines exactly the number of electrons N, the ground-state wavefunction $\Psi[\rho_0(\mathbf{r})]$ and all other electronic properties [18]. The second theorem asserts: *The electron density that minimizes the energy of the overall functional is the true electron density corresponding to the full solutions of the Schrödinger equation* [27]. This implies that the ground-state electron density can be obtained by minimizing the energy with respect to the electron density. However, neither theorems provides a direct method for determining the ground-state density $\rho_0(\mathbf{r})$; this is where the Kohn-Sham approach becomes essential.

Kohn and Sham took a different approach considering a fictitious system of non-interacting electrons that reproduces the same electron density as the real system of interacting electrons. In this new scheme it is assumed that the density $\rho_0(\mathbf{r})$ can be represented in terms of what are usually called Kohn-Sham (KS) orbitals $\phi_j(\mathbf{r})$ [23], which represent the wave functions of the non-interacting particles in this fictitious system, i.e.,

$$\rho_0(\mathbf{r}) = \sum_j |\phi_j(\mathbf{r})|^2 \tag{2.2}$$

With the Kohn-Sham (KS) formulation of DFT, the total energy is given by

$$E_{\text{tot}}^{\text{KS}-\text{DFT}} = -\frac{1}{2}\sum_i \int \phi_i^*(\mathbf{r})\nabla^2\phi_i(\mathbf{r})d^3r - \sum_A \int \frac{Z_A}{|\mathbf{r}-\mathbf{R}_A|}\rho_0(\mathbf{r})d^3r$$

$$+ \frac{1}{2}\iint \frac{\rho_0(\mathbf{r})\rho_0(\mathbf{r}')}{|\mathbf{r}-\mathbf{r}'|}d^3rd^3r' + E_{\text{xc}} + \frac{1}{2}\sum_{A\neq B}\frac{Z_AZ_B}{|\mathbf{R}_A-\mathbf{R}_B|} \quad (2.3)$$

where the terms on the right-hand side correspond to: the non-interacting kinetic energy of the electrons, the electrons-nuclei attraction energy, the classical Coulomb electron-electron repulsive energy, the exchange-correlation energy (accounting for the remaining electronic energy not included in the non-interacting kinetic and electrostatic terms), and the nuclei-nuclei repulsion energy, respectively. The KS orbitals, $\phi_j(\mathbf{r})$, and the electronic density, ρ_0, used to evaluate $E_{\text{tot}}^{\text{KS}-\text{DFT}}$, are obtained by solving self-consistently the KS equations:

$$\left[-\frac{1}{2}\nabla^2 - \sum_A \frac{Z_A}{|\mathbf{r}-\mathbf{R}_A|} + \int \frac{\rho_0(\mathbf{r}')}{|\mathbf{r}-\mathbf{r}'|}d^3r' + v_{\text{xc}}(\mathbf{r})\right]\phi_i(\mathbf{r}) = \epsilon_i\phi_i(\mathbf{r}) \qquad (2.4)$$

The only terms in Eq.2.3 and Eq.2.4 that are not known exactly are E_{xc} and $v_{\text{xc}}(\mathbf{r}) = \delta E_{\text{xc}}/\delta\rho_0$. Therefore, the accuracy of the calculated properties depends significantly on the approximations used for E_{xc} and $v_{\text{xc}}(\mathbf{r})$ [18]. There are numerous approximations available for the exchange and correlation terms; in this study, we employ the Perdew–Burke–Ernzerhof (PBE) exchange-correlation functional, which is widely used in quantum mechanics and computational chemistry [28], [29], [30].

A schematic representation of the self-consistent process for solving Eq.2.4 is shown in Fig.2.1.

1. An initial guess of the electron density $\rho^{(0)}(\mathbf{r})$ is provided.

Repeated until the density converges to a self-consistent solution.

2. The potentials $v_H(\mathbf{r})$ and $v_{xc}(\mathbf{r})$ corresponding to $\rho^{(0)}(\mathbf{r})$ are constructed.

3. The Kohn-Sham equations are solved to obtain the $\phi_i(\mathbf{r})$ orbitals.

4. A new density $\rho^{(1)}(\mathbf{r})$ is calculated from the $\phi_i(\mathbf{r})$.
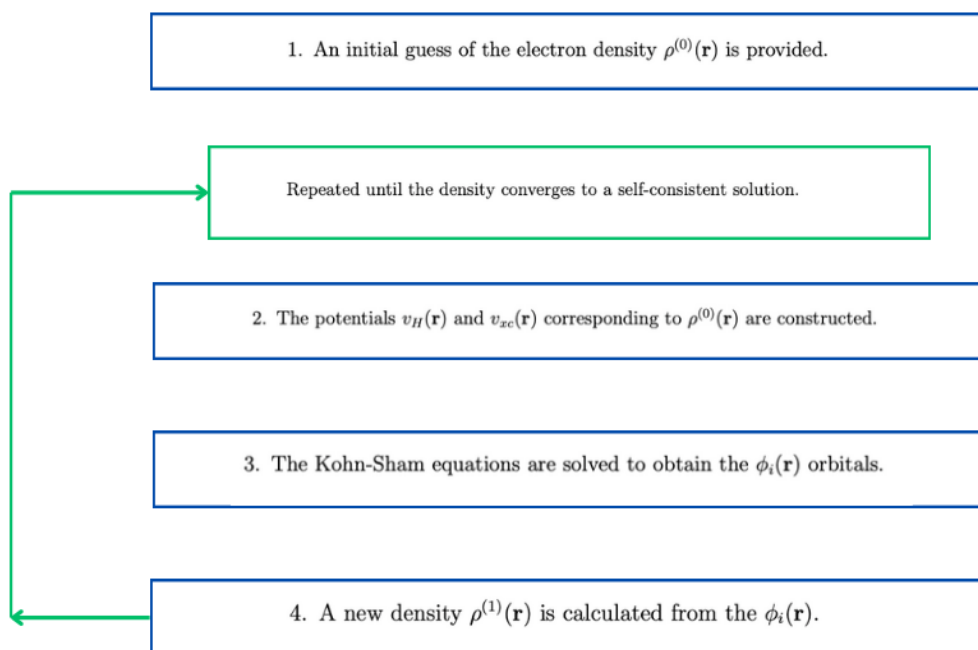
Figure 2.1: Self-consistent squeme to solve KS equations

This summarizes the essence of DFT and underscores its significant role in addressing quantum-mechanical problems. However, it is important to acknowledge one of the major limitations in applying DFT-based methods to true materials design: the incorporation of temperature-driven effects [18], [31]. To address this issue, incorporating DFT into the Molecular Dynamics (MD) method is essential, as it offers valuable insights into energy calculations and structural equilibrium properties [24].

2.2   Introduction to Molecular Dynamics

Among the various approaches used to study many-body systems in condensed matter physics through computational simulation, molecular dynamics stands out as one of the simplest methods [13]. Given its significance, it is necessary to briefly explain the fundamentals of molecular dynamics, its limitations, and how the application of DFT to molecular dynamics led to a groundbreaking approach that addressed the challenge of solving the electronic structure of large systems in solid-state physics [14].

2.2.1   Classical Molecular Dynamics

Classical molecular dynamics, commonly referred to as Molecular Dynamics (MD), is a simulation technique that originated in 1957 with the pioneering work of Alder and Wainwright. Their method aimed to solve the classical equations of motion for several hundred particles simultaneously by utilizing fast electronic computers [32]. Thanks to the accelerating advance of available computational power as well as increasingly sophisticated approaches, MD methods have become more and more popular in the research community seeking to simulate materials at molecular and atomic scales. [33]

In MD, Newton's equations of motion are solved numerically, with atomic interactions described by predefined potentials, which are derived either from experimental data or from independent electronic structure calculations [22]. Some well-known potentials include Lennard-Jones, Morse, Yukawa, Coulomb, gravita-

tional, and Buckingham potentials [33].

Now, how reliable is MD in terms of obtaining useful and verifiable information from a system? The reliability of MD is based on the ergodicity hypothesis introduced by Boltzman. This hypothesis posits that: *For large systems of interacting particles in equilibrium, i.e. for an appropriate microcanonical ensemble (NVE), the time averages are close to the ensemble average.* [34] Mathematically, a system is said to be ergodic if,

$$\langle A \rangle_{\text{ens}} = \frac{\int_0^{t_{\text{tot}}} dq A(q) p(q)}{\int_0^{t_{\text{tot}}} dq p(q)} \cong \lim_{t_{\text{tot}} \longrightarrow \infty} \frac{1}{t_{\text{tot}}} \int_0^{t_{\text{tot}}} dt A(q(t)) = \langle A \rangle_{\text{time}} , \qquad (2.5)$$

In this context, A represents an observable thermodynamic variable, q represents a microstate of the system, $p(q)$ is the associated probability distribution function, and t_{tot} indicates the temporal evolution of the system that when extended to infinity ($t_{tot} \longrightarrow \infty$) equals the ensemble average $< A >_{ens}$ and the time average $< A >_{time}$. This principle arises from Newton's equations of motion, which ensure the conservation of total energy E. However, in certain situations, it becomes necessary to consider other statistical ensembles, such as the constant volume-constant temperature (NVT) ensemble or the constant pressure-constant temperature (NpT) ensemble. This is achievable by coupling the system to a "thermostat" or "barostat" [35]. Given the relevance of the introduction of a thermostat to our case study, a brief discussion of what a thermostat is, along with a description of the specific Nosé-Hoover thermostat employed, is warranted.

Nosé-Hoover thermostat

To create a scheme in MD that enables the generation of thermodynamic ensembles at constant temperature, it is necessary to introduce a thermostat algorithm [36]. For our purposes, where a canonical ensemble (NVT) is required, we employed the Nosé-Hoover thermostat. This choice is based on its proven effectiveness for simulations involving this type of ensemble [37], [38], [39].

The Nosé-Hoover algorithm achieves the exact reproduction of an NVT ensemble by extending the Lagrangian of the system with an additional "dummy" variable ζ, which is associated with a "mass" Q [35]. This extension introduces a "friction" term into Newton's equations of motion, resulting in:

$$\ddot{\vec{r}}_i = \vec{f}_i/m_i - \zeta\,\dot{\vec{r}}_i \tag{2.6}$$

where $\vec{r}_i$ represents the position of particle i, m_i is the mass of particle i, and $\vec{f}_i$ is the force acting on particle i. The equation for the fluctuation of the friction coefficient ζ over time is given by:

$$\frac{d\zeta}{dt} = \frac{1}{Q}\left[\sum_{i=1}^{N} m_i\,\dot{\vec{r}}_i^2 - 3(N+1)k_BT\right] \tag{2.7}$$

where $N+1$ is the number of degrees of freedom of the system as there is one more variable ζ to consider, k_B is the Boltzman constant, and T is the target temperature. Note how the heat exchange between the system and its surroundings

exhibits oscillatory behavior as described by the sign of $\frac{d\zeta}{dt}$. When $\frac{d\zeta}{dt} < 0$, heat flows into the real system, and when $\frac{d\zeta}{dt} > 0$, heat flows out of the real system. [36]

2.2.2   Ab initio Molecular Dynamics

At this point, it is important to remind: it is quantum mechanics that describes the basic physics of condensed matter, and not classical mechanics. However, solving the Schrödinger equation for systems with numerous nuclei and electrons is computationally infeasible, even with the most advanced computational resources [35]. To address this challenge, the Ab-initio Molecular Dynamics (AIMD) method has emerged as a popular approach [15]. This method involves calculating the forces acting on the nuclei using DFT calculations performed "on the fly" as the molecular dynamics trajectory evolves [22]. In AIMD, electronic variables are treated as active degrees of freedom rather than being integrated beforehand, which provides a significant advantage over classical methods by eliminating the need for a predefined potential [40].

The AIMD method was initially applied using the pseudopotential approach, which replaces the all-electron potential with a smoother potential that implicitly accounts for core electrons [16]. The subsequent advancement aimed to integrate AIMD with augmented wave methods, introducing the projector-augmented wave (PAW) method developed by Blöchl [16]. This method combines the computational efficiency of pseudopotentials with the accuracy of the full potential linearized augmented plane wave (FLAPW) method, which is often considered the benchmark for DFT calculations in solids [17]. A more comprehensive explanation of the PAW

method is beyond the scope of this study.

A summary diagram illustrating the process of an AIMD calculation using the PAW method is presented in Fig.2.2.
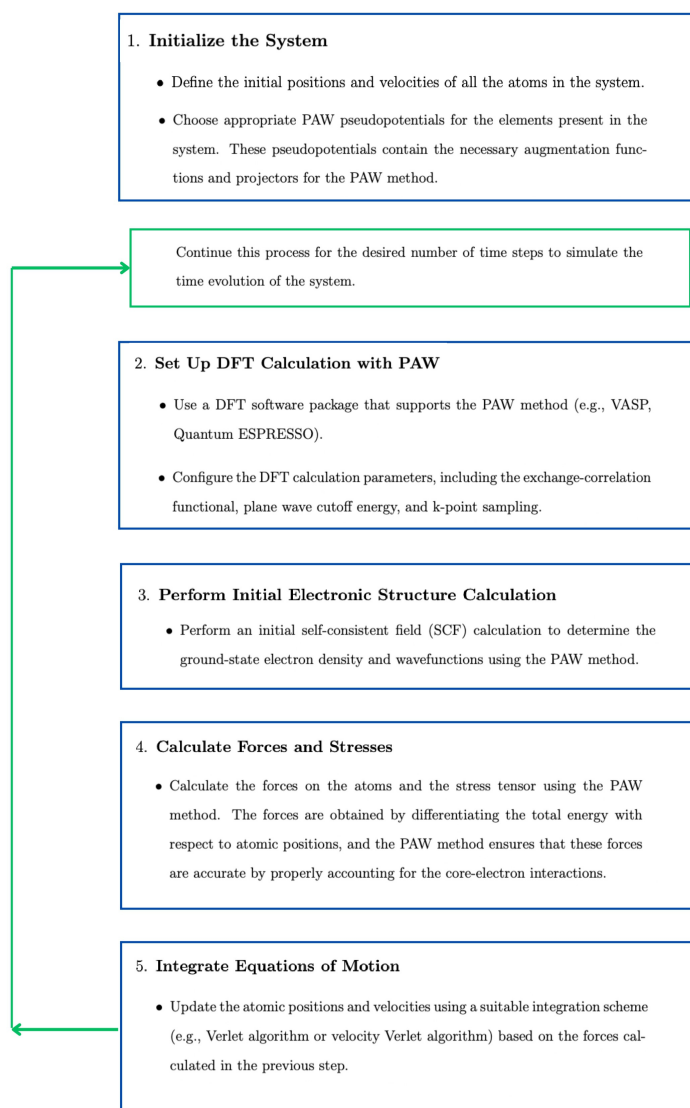
Figure 2.2: Process of an AIMD calculation using the PAW method

2.3 Schottky junction and thermal current transport process

2.3.1 Schottky junction

The metal-semiconductor junction (MSJ) can result in two distinct types of devices: an ohmic junction or a rectifying junction, the latter also known as a Schottky junction [2]. For MSJ rectifiers, a significant advancement in understanding their behavior was the identification of a potential barrier at the metal-semiconductor interface [41]. Subsequently, Schottky and Mott developed a more refined theoretical model to explain the barrier height. According to this model, the barrier height is determined by the difference between the work functions of the metal and the semiconductor [42]. The work function is defined as the energy difference between the vacuum level E_0 and the metal Fermi level E_{FM}. For metals it is denoted by $q\phi_m$, while for semiconductors, it is expressed as $q\phi_s = q(\chi + \phi_n)$, where $q\chi$ is the electron affinity measured from the bottom of the conduction band E_C to E_0, and $q\phi_n$ is the energy difference between E_C and the semiconductor Fermi level E_{FS}.

Considering a scenario where a metal and a semiconductor are initially isolated from each other, as depicted in Fig.2.3a, and then brought into contact, it is observed that the electrons in the semiconductor's conduction band, possessing higher energy than those in the metal, flow towards the metal. This electron flow continues until the Fermi levels on both sides equalize, establishing a nega-

tive charge on the metal side. Additionally, the departure of electrons from the semiconductor's conduction band leaves behind ionized, positively charged donors, which creates a positive charge on the semiconductor side. This results in the formation of an electric field directed from the semiconductor to the metal. Consequently, the reduction in the concentration of free electrons near the semiconductor junction leads to an increase in the separation between the conduction band edge E_C and the Fermi level E_F. In this thermally equilibrated system, E_F remains constant throughout, but the conduction band edge E_C curves upwards, as shown in Fig.2.3b. Furthermore, there is no change in the semiconductor's band gap upon contact with the metal, as the valence band edge E_v bends parallel to the conduction band edge E_C. The vacuum level E_0 of the semiconductor will follow the same curvature as E_C, since χ is known to be a constant quantity. [2]
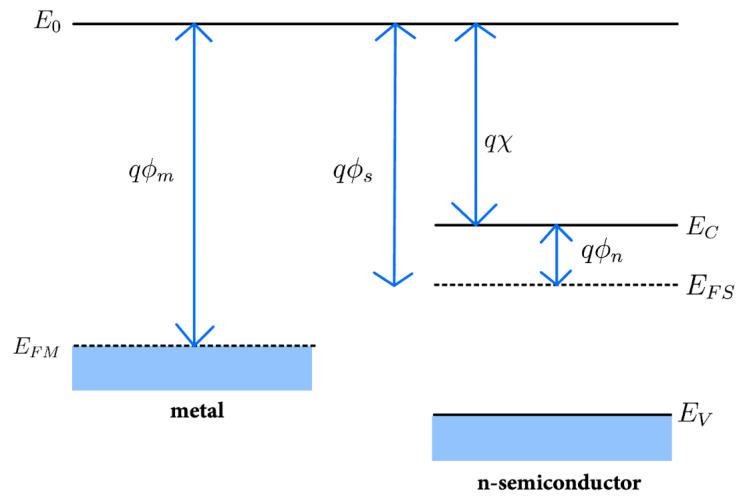
(a) Isolated materials
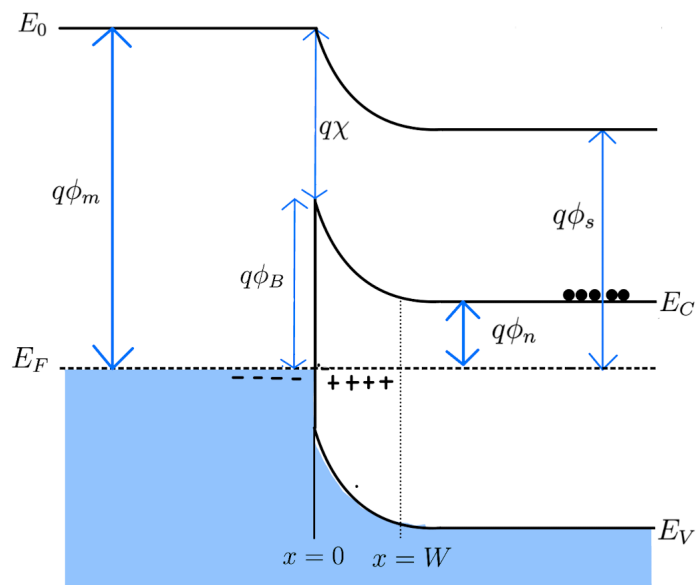
(b) Thermal equilibrium situation after the contact has been made

Figure 2.3: Energy electric band diagram of metal contact to n-type semiconductor

An essential condition for determining the barrier height is the continuity of the vacuum level E_0 throughout the transition region. Consequently, the degree of band bending is equal to the difference between the two vacuum levels, which corresponds to the difference between the two work functions:

$$qV_i = q(\phi_m - \phi_s) \tag{2.8}$$

Here, V_i is known as contact potential difference, and qV_i represents the potential barrier that an electron must overcome to move from the semiconductor to the metal. The barrier for electrons moving in the opposite direction, from the metal to the semiconductor, is different and is given by:

$$\phi_B = (\phi_m - \chi) \tag{2.9}$$

Equation (2.8), established independently by Schottky [41] and Mott [43], is specific for n-type semiconductor.

2.3.2 Thermionic-Emission Theory

Having established how the potential barrier is formed and quantified, the next step is to understand the current transport mechanisms in these devices. Various theories describe the current transport processes under forward bias (with inverse processes occurring under reverse bias) [44]. However, the theory most relevant to

our case study is the Thermionic Emission Theory (TET). In the context of semi-conductors, this theory is particularly applicable to metal-semiconductor contacts and heterostructures where there is a significant energy band offset. Under such conditions, electrons can overcome the energy barrier and flow from the metal into the semiconductor when exposed to elevated temperatures. The theory is based on the following assumptions: (1) The barrier height ϕ_B is much larger than KT, (2) thermal equilibrium is established at the emission site, and (3) the net current flow results from the combination of two separate current flows—one from the metal to the semiconductor and another from the semiconductor to the metal [44]. Based on these assumptions, the total Thermionic-Emission current density is expressed as:

$$J_n = A^* T^2 \exp\left(-\frac{q\phi_B}{K_B T}\right)\left[\exp\left(\frac{qV}{K_B T}\right) - 1\right] = J_{TE}\left[\exp\left(\frac{qV}{K_B T}\right) - 1\right] \quad (2.10)$$

where A^* is the Richardson constant, T is the absolute temperature, K_B is the Boltzmann constant, V is the applied voltage, and J_{TE} is the saturation current density for the Thermionic-Emission Theory.

Chapter 3

Models and Methods

3.1 Model

To perform MD calculations, it was necessary to construct a starting model of a G/S SJ that closely mimicked the conformation likely to be found in an experimental setup.

The model was based on an extension of the unit cell of a silicon crystal structure with a surface cut oriented in the [100] direction, known as the most stable Si surface. The model consisted of 8 layers of silicon, with extension factors of 3 and 5 in the a and b directions, respectively. This resulted in a supercell model containing 120 Si atoms (see Fig.3.1a). Subsequently, a monolayer graphene sheet composed of 80 carbon atoms was placed onto the silicon supercell to form the G/S SJ model (see Fig.3.1b). To address the strain forces resulting from atomic

interactions at the Si-C interface, a subsequent structure optimization process was conducted without imposing any symmetry or geometry constraints (see Fig.3.1c). For this process it was decided to use version 5.4.4 of VASP which is known to be reliable due to the study conducted by Paredes & Beltrán [21]. Dispersive forces were accounted for using a Grimme-like pairwise potential. The energy cutoff (EN-CUT) for the SCF calculations was set to 450 eV, with default values for structure optimization control parameters.

The equilibrium Si-C model obtained was an almost rectangular cell with dimensions $a = 12.074945$ Å, $b = 17.502307$ Å, and $c = 21.364605$ Å, where a vacuum of approximately 9 Å was included along the c direction (see Fig.3.1d for a top-side view of the model). Moreover, the distance between the Si surface and the graphene sheet was approximately 3.4 Å. A CIF file containing the model is available in the Appendix A.

Ensuring a well-relaxed initial structure was crucial for achieving faster convergence in the self-consistent field calculations at each time step of the AIMD simulation. Additionally, this approach provided stability to the simulation by minimizing high-energy configurations that could cause numerical instabilities.

(a) Side view of the silicon bulk

(b) Side view of the unoptimized G/S SJ model

(c) Side view of the optimized G/S SJ model

(d) Top side view of the G/S SJ model
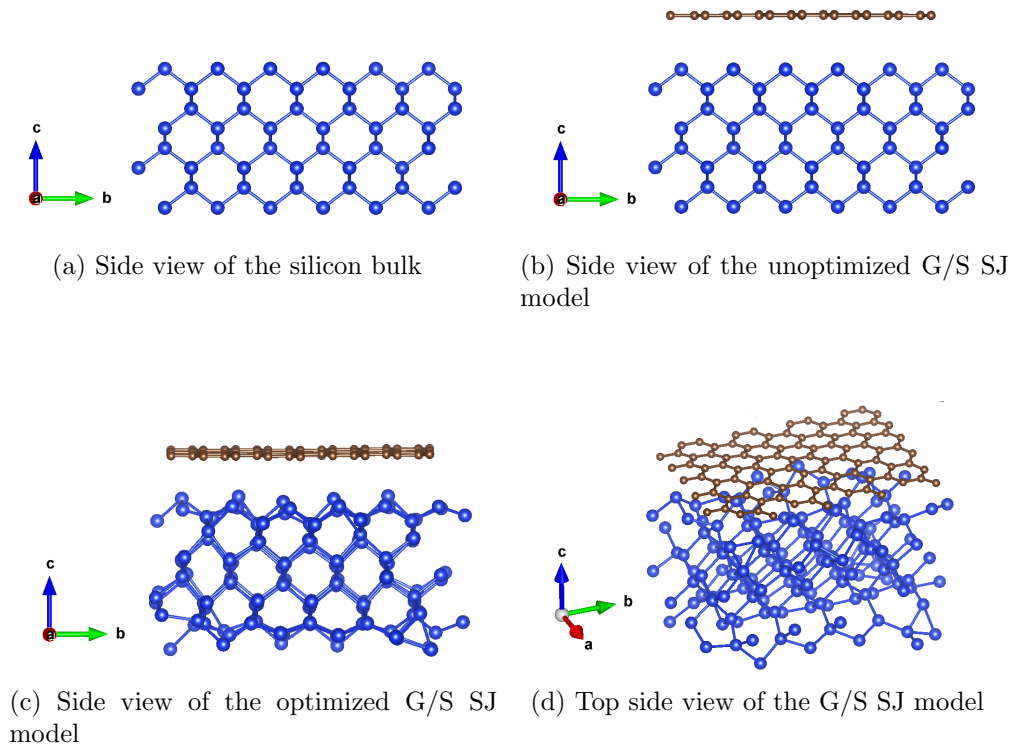
Figure 3.1: G/S SJ model creation process

3.2 Methods

3.2.1 Validation of methods in VASP version 6.4.2

As a preliminary objective before developing the AIMD protocol, the methods implemented in VASP version 6.4.2 were validated. This version of VASP was chosen because it allows for the incorporation of temperature effects into our system, making it essential to verify its accuracy through an analysis similar to that conducted by Paredes & Beltrán [21]. Specifically, the goal was to confirm that

the known effects on the electronic properties of the device—resulting from variations in the distance between the graphene sheet and the silicon bulk—could be reproduced using VASP version 6.4.2.

We began with the initial G/S SJ model and varied the silicon-graphene distance. This adjustment was made by modifying the POSCAR file, which contains the atomic positions of the system and is one of the four essential files required for a VASP calculation. In the POSCAR file, the positions of the silicon atoms were kept constant, while the distances along the c-axis for the carbon atoms were manually adjusted. Five scenarios were evaluated: (1) reducing the distance by 10% of the original value up to 3.06 Å, (2) reducing the distance by 20% of the original value up to 2.72 Å, (3) at the original distance 3.4 Å, (4) increasing the distance by 10% of the original value up to 3.74 Å, and (5) increasing the distance by 20% of the original value up to 4.08 Å.

The INCAR file, which defines the calculation parameters, was also modified. This file was based on the one used previously during the structural optimization for the construction of the starting model and was adapted to accommodate VASP version 6.4.2. Specifically, the energy cutoff (ENCUT) was reduced from 450 eV to 200 eV, the electronic minimization algorithm (ALGO) was changed from Fast to VeryFast, the ionic relaxation algorithm (IBRION) was altered from 1 to 2, and the ionic step size (POTIM) was increased from 0.2 to 0.5. These adjustments reduced computational time and resource usage without compromising the accuracy of the calculations.

For the remaining two files, KPOINTS and POTCAR, we used those from

the structural optimization process without any modifications. The KPOINTS file configured a mesh centered on the Γ point, with 4 points in the a and b directions, and 2 points in the c direction. This configuration is standard for a system that exhibits more variation in the ab plane and less in the c direction. For the POTCAR file, we utilized the available pseudopotentials in VASP, specifically PAW potentials, selecting those corresponding to Si and C.

Using these four files, structural optimization calculations for the G/S SJ model were conducted across the five scenarios. In all cases, the positions of the C atoms were fixed, while the Si atoms were allowed to move freely, enabling the system to relax into a stable energy configuration. The resulting structures were then loaded into QuantumATK for the computation of electronic properties such as the band structure, effective mass, and Fermi level.

3.2.2 Development and implementation of an AIMD protocol

The development and implementation of the AIMD protocol were divided into two phases. The first phase focused on introducing the effect of absolute temperature into the initial G/S SJ model. This was accomplished through an AIMD calculation that allowed the system to reach thermal equilibrium. In the second phase, an output G/S SJ structure was selected to serve as new input data for the atomic positions in a subsequent AIMD calculation. This final calculation was performed to isolate the model, enabling it to evolve dynamically without energy exchange.

The first phase began with the modification of the INCAR file used during the validation process, with additional parameters appended to the end of the file:

Selected parameter	Description
IBRION = 0	Specifies that a molecular dynamics calculation will be performed instead of a standard structural relaxation.
NSW = 10000	Defines the total number of ionic steps to be executed.
POTIM = 5.0	Defines the time step (in femtoseconds) for each AIMD step.
MDALGO = 2	Specifies the use of the Nosé-Hoover thermostat to maintain constant temperature during the simulation.
TEBEG = 300	Initial simulation absolute temperature. Here, the simulation starts at 300 K.
TEEND = 300	Final absolute temperature of the simulation. Keeping the same value as TEBEG ensures that the temperature remains constant.
ISIF = 2	Specifies that only ion positions will be updated, keeping cell shape and volume constant, which is suitable for NVT ensemble simulations.

Table 3.1: Added parameters for the first phase (emulating an NVT assembly) of the AIMD protocol

During this phase, the POTIM value was varied across 5.0, 7.0, 8.0, 9.0, and 10.0 to accelerate the thermalization of the system. However, it was found that values greater than 5.0 resulted in overestimated forces, causing the simulation to crash or terminate with an error.

In the second phase, the INCAR file from the first phase served as the starting point. To adapt it for this phase, the following parameters were modified:

Once the second phase was correctly executed, the system was allowed to evolve

Selected parameter	Description
MDALGO = 1	Specifies the use of the Andersen thermostat for the simulation. This algorithm is simpler than Nosé-Hoover and is often employed in NVE or NVT simulations to control the temperature.
ANDERSEN_PROB = 0.0	Sets the collision probability in the Andersen thermostat. A value of 0.0 effectively turns off collisions, making this an NVE ensemble calculation (no energy exchange with the environment, keeping the total energy constant).

Table 3.2: Modified parameters for the second phase (emulating an NVE assembly) of the AIMD protocol

for a total of 1000 ionic steps. Then, from the output file XDATCAR containing the evolution of the atomic positions of the G/S SJ model, the structures were extracted every 50 ionic steps until reaching 1000, which gave us a total of 20 representative structural samplings for the subsequent calculation of electronic structure parameters. This process was repeated a total of three times for temperatures of 300K, 400K and 500K.

3.2.3 Characterizing of the G/S SJ

The 20 G/S SJ representative structural samplings corresponding to a given temperature were loaded into QuantumATK for the computation of their electrical properties, such as the Fermi level and effective mass. For each of these structural samplings, a specific value for the electrical properties was obtained, corresponding to the atomic positions at a given step. As previously mentioned, in MD calculations, the information obtained is based on the ergodicity principle. Therefore,

the primary interest lies in the average values of the electronic properties across the 20 structural samplings, as these averages represent the values to which the system is expected to converge if allowed to evolve over a sufficiently long period.

As a result, for each G/S SJ model subjected to a specific temperature, two average values were obtained: the Fermi level and the effective mass. These averaged values were subsequently used as input parameters for a graphene/silicon Schottky interface model, designed within the Sentaurus software, enabling device-level simulations and the generation of an IV curve. For more detailed information on the model implemented in Sentaurus refer to the study conducted by Paredes & Beltrán [21].

Chapter 4

Results

4.1 Results of method validation in VASP version 6.4.2

The band structures obtained for the five cases of graphene displacement considered in this study are shown in Fig.4.1. For comparison, the band structures for the three cases of graphene displacement from the study conducted by Paredes & Beltrán [21], previously mentioned, are shown in Fig.4.2.
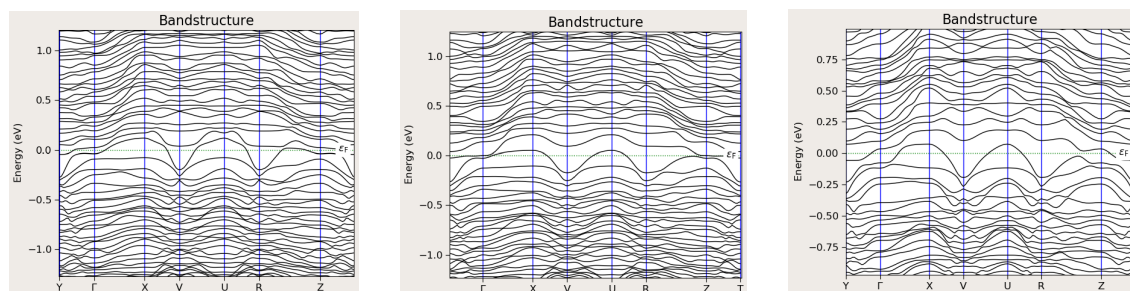
(a) -20% distance displacement up to 2.72 Å

(b) -10% distance displacement up to 3.06 Å

(c) original distance 3.4 Å
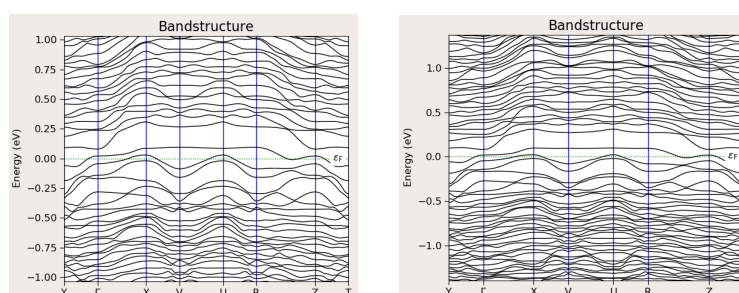
(d) +10% distance displacement up to 3.74 Å

(e) +20% distance displacement up to 4.08 Å

Figure 4.1: Band structure for the five distance scenarios of the G/S SJ
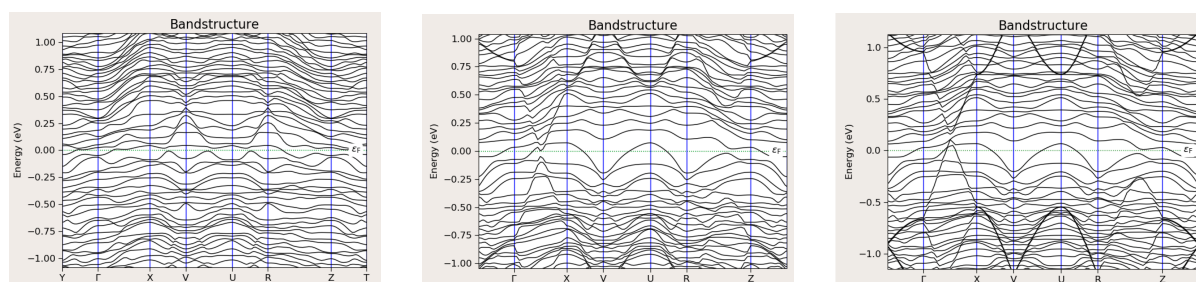
(a) -1 Å distance displacement up to 0.45 Å

(b) original distance 1.45 Å

(c) +2.5 Å distance displacement up to 3.95 Å

Figure 4.2: Band structure for the three distance scenarios of the G/S SJ obtained by Paredes & Beltrán

In both Fig.4.1 and Fig.4.2, a similar effect is observed in the bandgap in response to changes in the distance between the graphene sheet and the silicon bulk. Specifically, when the graphene sheet is brought closer to the silicon bulk, the bandgap is reduced, suggesting that the overall configuration exhibits more metallic behavior, as it facilitates the passage of electrons from the valence band to the conduction band. Conversely, when the graphene sheet is moved away from the silicon bulk, the bandgap increases, leading to less metallic behavior, as it becomes more difficult for electrons to transition from the valence band to the conduction band.

This behavior is also reflected in the Fermi level and effective mass values obtained in both studies, as shown in Table.4.1 and Table.4.2. As the graphene sheet approaches the silicon bulk, the Fermi level becomes less negative, and the effective mass decreases. Conversely, as the graphene sheet is moved away, the Fermi level becomes more negative, and the effective mass increases.

One inconsistency in this trend is observed in the original case of our validation study, where a slight increase of 0.008 eV in the Fermi level is noted relative to the case with a 10% reduction in distance. While this inconsistency appears in the Fermi level, the effective mass continues to follow the expected trend. This introduces an important consideration: determining whether a material exhibits more or less metallic behavior depends on the collective evaluation of electronic properties, not just one.

Thus, the increase of 0.008 eV in the Fermi level can be interpreted as an increase in the maximum energy that can be occupied by electrons in the system.

This suggests that the energy states available for conduction are closer to the conduction band, potentially indicating a more metallic behavior. However, the simultaneous increase in the effective mass implies a reduction in electron mobility, which could offset the small increase in the Fermi level, leading to less metallic behavior overall. This interpretation is supported by the band structures presented in Fig.4.1.

Configuration	Fermi level [eV]	Effective mass [u]
-20% distance displacement up to 2.72 Å	-4.442	0.517
-10% distance displacement up to 3.06 Å	-4.460	0.666
original distance 3.4 Å	-4.452	0.823
+10% distance displacement up to 3.74 Å	-4.492	3.202
+20% distance displacement up to 4.08 Å	-4.494	4.032

Table 4.1: Fermi level and effective mass for the five distance scenarios of the G/S SJ

Configuration	Fermi level [eV]	Effective mass [u]
-1 Å distance displacement up to 0.45 Å	-4.615	0.187
original distance 1.45 Å	-4.782	0.859
+2.5 Å distance displacement up to 3.95 Å	-4.8152	0.882

Table 4.2: Fermi level and effective mass for the three distance scenarios of the G/S SJ obtained by Paredes & Beltrán

4.2 Results of the characterization of the G/S SJ at different temperatures

The calculated averages of the electronic properties for the G/S SJ model subjected to different temperatures are summarized in Table.4.3.

Configuration	Fermi level [eV]	Effective mass [u]
300K	-4.743	0.888
400K	-4.775	1.083
500K	-4.759	0.897

Table 4.3: Fermi level and effective mass of the G/S SJ model subjected to three different temperatures (300K, 400K, 500K)

It is noteworthy that the electronic properties results for the G/S SJ presented in Table.4.3 do not clearly illustrate the effects of temperature on the device's behavior. The variations in both the Fermi level and effective mass show changes that appear insignificant and lack a clear trend. However, it is important to remember that these electronic property values were obtained to subsequently feed into a model implemented in Sentaurus. This model simulates the graphene/silicon Schottky interface at the device level, using the finite element method to solve a series of equations that require specific initial approximations. For further details, it is recommended to consult the documentation of the study conducted by Paredes & Beltrán [21], where the model design code is provided. Using the parameters from Table.4.3, three current-voltage (IV) characteristic curves were obtained (see Fig.4.3).
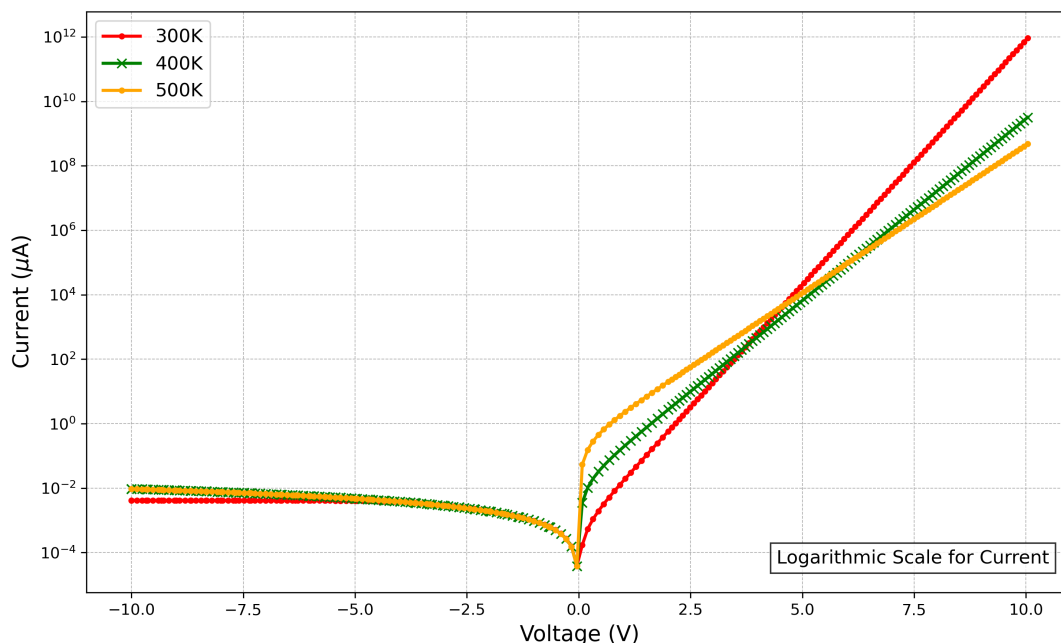
Figure 4.3: Current–voltage characteristic of the G/S SJ model subjected to three different temperatures (300K, 400K, 500K)

It can be observed that under forward bias, increasing the temperature initially leads to an increase in the material's conductivity. However, as the voltage increases, this relationship reverses, with higher temperatures leading to a reduction in conductivity. This behavior is consistent with the theoretical descriptions of thermionic emission. By substituting the relevant parameters into equation (2.10), we can generate two graphs that illustrate thermionic current as a function of temperature (see Fig.4.4).

As shown in Fig.4.4a, at a sample voltage of V=0.5 V, the increase in temperature corresponds to an increase in the material's conductivity, consistent with the trend observed in Fig.4.3. Similarly, as depicted in Fig.4.4b, at a sample voltage of V=5.0 V, the increase in temperature corresponds to a decrease in conductivity,
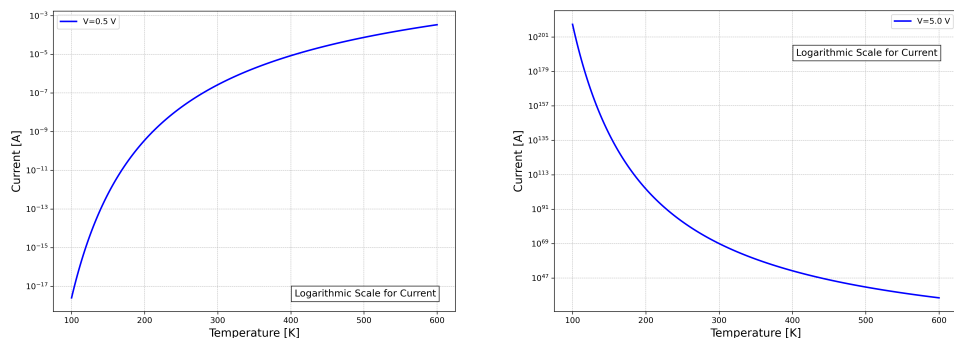
(a) Thermionic current as a function of temperature for V=0.5 V

(b) Thermionic current as a function of temperature for V=5.0 V

Figure 4.4: Thermionic current as a function of temperature

reflecting the behavior shown in Fig.4.3. Thus, the results obtained support the hypothesis presented at the beginning regarding the indirect relationship between temperature and electronic properties: temperature-induced modifications in the atomic structure of the G/S SJ subsequently altering its electronic behavior.

Chapter 5

Conclusions

In this study, the previous analysis conducted by Paredes & Beltrán [21] was extended. Their initial study, using quantum-mechanical and device-level simulations, established that variations in the geometry of the G/S SJ correlated with changes in its electronic properties. Recognizing the need for a more comprehensive characterization of the G/S SJ, it was deemed essential to introduce a temperature parameter into the system. The hypothesis proposed that there is an indirect relationship between temperature and electronic properties, meaning that temperature-induced modifications in the atomic structure of the G/S SJ would subsequently alter its electronic behavior. To investigate this, three objectives were established and successfully met in the thesis.

The first objective was to validate the methods in VASP version 6.4.2 by replicating the analysis of the dependence of the graphene-silicon distance on its electronic properties, as previously performed by Paredes & Beltrán.

The second objective involved developing an AIMD protocol that allowed for the thermalization of an optimized G/S SJ model using a Nosé–Hoover thermostat, followed by a dynamic evolution of the system without energy exchange. Representative structural samplings were extracted from this non-equilibrium dynamic process at three different temperatures (300K, 400K, 500K).

The third objective focused on characterizing the G/S SJ by loading the representative structural samplings corresponding to each temperature into QuantumATK to compute electronic properties such as the Fermi level and effective mass. The average values of these electronic properties were then used as input parameters for a graphene/silicon Schottky interface model designed in Sentaurus, enabling device-level simulations and the generation of an IV curve.

The IV characterization curves of the G/S SJ presented in Fig.4.3 support the initial hypothesis regarding the indirect relationship between temperature and electronic properties. Building on the findings of Paredes & Beltrán, which demonstrated that geometric variations in the G/S SJ lead to changes in its electronic properties, this study extends the analysis to show that the temperature to which the G/S SJ is subjected also results in significant alterations in its electronic behavior.

Bibliography

[1] A. K. Geim. Graphene: status and prospects. *Science*, 324(5934):1530–1534, 2009.

[2] A. Di Bartolomeo. Graphene schottky diodes: An experimental review of the rectifying graphene/semiconductor heterojunction. *Physics Reports*, 606:1–58, 2016.

[3] H. Selvi, E. W. Hill, P. Parkinson, and T. J. Echtermeyer. Graphene–silicon-on-insulator (gsoi) schottky diode photodetectors. *Nanoscale*, 10(40):18926–18935, 2018.

[4] C. C. Chen, M. Aykol, C. C. Chang, A. F. J. Levi, and S. B. Cronin. Graphene-silicon schottky diodes. *Nano Letters*, 11(5):1863–1867, 2011.

[5] et al. Selvi, Hakan. Towards substrate engineering of graphene–silicon schottky diode photodetectors. *Nanoscale*, 10(7):3399–3409, 2018.

[6] et al. Hussin, Mohd Rofei Mat. Fabrication and characterization of graphene-on-silicon schottky diode for advanced power electronic design. *Sains Malaysiana*, 46(7):1147–1154, 2017.

[7] et al. Wang, Yiming. The fabrication of schottky photodiode by monolayer graphene direct-transfer-on-silicon. *Journal of Applied Physics*, 128(1), 2020.

[8] T. Zhang, Q. Xue, S. Zhang, and M. Dong. Theoretical approaches to graphene and graphene-based materials. *Nano Today*, 7(3):180–200, 2012.

[9] Zak E. Hughes and Tiffany R. Walsh. Computational chemistry for graphene-based energy applications: progress and challenges. *Nanoscale*, 7(16):6883–6908, 2015.

[10] Mahesh P. More and Prashant K. Deshmukh. Computational studies and biosensory applications of graphene-based nanomaterials: A state-of-the-art review. *Nanotechnology*, 31(43):432001, 2020.

[11] Naman. Verma, Akarsh. Jain and Sushanta K. Sethi. *Modeling and simulation of graphene-based composites*, pages 167–198. Woodhead Publishing, 2022.

[12] P. Singh and M. K. Harbola. *Density-functional theory of material design: fundamentals and applications-I*. Oxford open materials science, 2021.

[13] K. Binder, J. Horbach, W. Kob, W. Paul, and F. Varnik. Molecular dynamics simulations. *Journal of Physics: Condensed Matter*, 16(5):S429, 2004.

[14] J. S. Tse. Ab initio molecular dynamics with density functional theory. *Annual Review of Physical Chemistry*, 53(1):249–290, 2002.

[15] R. Car and M. Parrinello. Unified approach for molecular dynamics and density-functional theory. *Physical Review Letters*, 55(22):2471, 1985.

[16] P. E. Blöchl, C. J. Först, and J. Schimpl. Projector augmented wave method: ab initio molecular dynamics with full wave functions. *Bulletin of Materials Science*, 26:33–41, 2003.

[17] D. J. Singh and L. Nordstrom. *Planewaves, Pseudopotentials, and the LAPW method.* Springer Science & Business Media, 2006.

[18] S. Datta and D. Jana. *Semiconductor physics: a density functional journey.* arXiv preprint, 2020.

[19] B. Leimkuhler and C. Matthews. Molecular dynamics. *Interdisciplinary Applied Mathematics*, 39(1), 2015.

[20] J. Hafner. Ab-initio simulations of materials using vasp: Density-functional theory and beyond. *Journal of Computational Chemistry*, 29(13):2044–2078, 2008.

[21] J. J. Paredes and D. K. Beltrán. Subthreshold model of interface graphene/silicon of schottky diode. *UNIVERSIDAD SAN FRANCISCO DE QUITO USFQ*, 2023.

[22] D. Marx and J. Hutter. Ab initio molecular dynamics: Theory and implementation. *Modern methods and algorithms of quantum chemistry*, 1:301–449, 2000.

[23] G. Colò. Density functional theory (dft) for atomic nuclei: a simple introduction. *Proceedings of the International School of Physics "Enrico Fermi*, 201:95–128, 2019.

[24] G. Jeanmairet, N. Levy, M. Levesque, and D. Borgis. Introduction to classical density functional theory by a computational experiment. *Journal of Chemical Education*, 91(12):2112–2115, 2014.

[25] L. J. Bartolotti and K. Flurchick. An introduction to density functional theory. *Reviews in computational chemistry*, pages 187–216, 1996.

[26] P. Hohenberg and W. Kohn. Inhomogeneous electron gas. *Physical Review*, 136(3B):B864, 1964.

[27] C. C. M. Rindt and S. V. Gaastra-Nedea. Modeling thermochemical reactions in thermal energy storage systems. *Advances in Thermal Energy Storage Systems*, pages 375–415, 2015.

[28] J. P. Perdew, K. Burke, and M. Ernzerhof. Generalized gradient approximation made simple. *Physical Review Letters*, 77(18):3865, 1996.

[29] B. H. L. B. Hammer, L. B. Hansen, and J. K. Nørskov. Improved adsorption energetics within density-functional theory using revised perdew-burke-ernzerhof functionals. *Physical Review B*, 59(11):7413, 1999.

[30] M. Ropo, K. Kokko, and L. Vitos. Assessing the perdew-burke-ernzerhof exchange-correlation density functional revised for metallic bulk and surface systems. *Physical Review B—Condensed Matter and Materials Physics*, 77(19):195445, 2008.

[31] T. Hickel, B. Grabowski, F. Körmann, and J. Neugebauer. Advancing density functional theory to finite temperatures: methods and applications in steel design. *Journal of Physics: Condensed Matter*, 24(5):053202, 2011.

[32] B. J. Alder and T. E. Wainwright. Phase transition for a hard sphere system. *The Journal of Chemical Physics*, 27(5):1208–1209, 1957.

[33] A. Shekaari and M. Jafari. A concise introduction to molecular dynamics simulation: theory and programming. *arXiv preprint*, page arXiv:2103.16944, 2021.

[34] D. Szász. Boltzmann's ergodic hypothesis, a conjecture for centuries? *Studia Scientiarum Mathematicarum Hungarica*, 31(1):299–322, 1996.

[35] K. Binder, J. Horbach, W. Kob, W. Paul, and F. Varnik. Molecular dynamics simulations. *Journal of Physics: Condensed Matter*, 16(5):S429, 2004.

[36] P. H. Hünenberger. Thermostat algorithms for molecular dynamics simulations. *Advanced Computer Simulation: Approaches for Soft Matter Sciences I*, pages 105–149, 2005.

[37] Q. Ke, X. Gong, S. Liao, C. Duan, and L. Li. Effects of thermostats/barostats on physical properties of liquids by molecular dynamics simulations. *Journal of Molecular Liquids*, 365:120116, 2022.

[38] Tatyana. Kuznetsova and Kvamme. Bj∅rn. Ergodicity range of nosé-hoover thermostat parameters and entropy-related properties of model water systems. *Molecular Simulation*, 21(4):205–225, 1999.

[39] et al. Huang, Cunkui. A novel method for molecular dynamics simulation in the isothermal–isobaric ensemble. *Molecular Physics*, 109(2):191–202, 2011.

[40] J. Hafner. Ab-initio simulations of materials using vasp: Density-functional theory and beyond. *Journal of computational chemistry*, pages 2044–2078, 2008.

[41] W. Schottky. Halbleitertheorie der sperrschicht. *Electronic Structure of Metal-Semiconductor Contacts*, pages 53–53, 1999.

[42] B. L. (Ed.) Sharma. *Metal-semiconductor Schottky barrier junctions and their applications.* Springer Science & Business Media, 2013.

[43] N. F. Mott. Note on the contact between a metal and an insulator or semiconductor. *Mathematical Proceedings of the Cambridge Philosophical Society*, 34(4):568–572, 1938.

[44] S. M. Sze, Y. Li, and K. K. Ng. *Physics of semiconductor devices.* John Wiley & Sons, 2021.

Appendix A

```
# CRYSTAL DATA
#------------------------------------------------
data_VESTA_phase_1


_chemical_name_common          'Interface C on Si <100> 120
    + 80 '
_cell_length_a                 12.074989
_cell_length_b                 17.502375
_cell_length_c                 21.364754
_cell_angle_alpha              89.686653
_cell_angle_beta               90.300735
_cell_angle_gamma              89.949677
_cell_volume                   4515.116560
_space_group_name_H-M_alt      'P 1'
_space_group_IT_number         1
```

```
loop_
_space_group_symop_operation_xyz
   'x, y, z'


loop_
   _atom_site_label
   _atom_site_occupancy
   _atom_site_fract_x
   _atom_site_fract_y
   _atom_site_fract_z
   _atom_site_adp_type
   _atom_site_U_iso_or_equiv
   _atom_site_type_symbol
   Si1     1.0    0.155909   0.004542    0.454547   Uiso ? Si
   Si2     1.0    0.101640   0.107351    0.390351   Uiso ? Si
   Si3     1.0    0.260529   0.104055    0.326084   Uiso ? Si
   Si4     1.0    0.267143   0.005438    0.256760   Uiso ? Si
   Si5     1.0    0.091982   0.023119    0.215162   Uiso ? Si
   Si6     1.0    0.083281   0.100670    0.126177   Uiso ? Si
   Si7     1.0    0.250306   0.053683    0.054498   Uiso ? Si
   Si8     1.0    0.183770   -0.040051   -0.022680  Uiso ? Si
   Si9     1.0    0.342718   0.007432    0.419624   Uiso ? Si
   Si10    1.0    0.837357   -0.002045   0.426902   Uiso ? Si
   Si11    1.0    0.414680   0.123521    0.392754   Uiso ? Si
```

```
Si12      1.0     0.724532    0.099170    0.397877    Uiso  ?  Si

Si13      1.0     0.572036    0.105664    0.328898    Uiso  ?  Si

Si14      1.0     0.916615    0.106488    0.352614    Uiso  ?  Si

Si15      1.0     0.582581    0.003363    0.261706    Uiso  ?  Si

Si16      1.0     0.922714    0.014262    0.270078    Uiso  ?  Si

Si17      1.0     0.427034    0.006726    0.194374    Uiso  ?  Si

Si18      1.0     0.755420    0.005933    0.209567    Uiso  ?  Si

Si19      1.0     0.415507    0.094962    0.108243    Uiso  ?  Si

Si20      1.0     0.759619    0.089471    0.124938    Uiso  ?  Si

Si21      1.0     0.601505    0.091512    0.059338    Uiso  ?  Si

Si22      1.0     0.925709    0.065559    0.070042    Uiso  ?  Si

Si23      1.0     0.498266   -0.013891    0.026454    Uiso  ?  Si

Si24      1.0    -0.025126   -0.031374   -0.026366    Uiso  ?  Si

Si25      1.0     0.176090    0.219920    0.424972    Uiso  ?  Si

Si26      1.0    -0.008878    0.422321    0.422274    Uiso  ?  Si

Si27      1.0    -0.013647    0.613194    0.429560    Uiso  ?  Si

Si28      1.0     0.192622    0.804478    0.423250    Uiso  ?  Si

Si29      1.0     0.080845    0.317827    0.376601    Uiso  ?  Si

Si30      1.0     0.083560    0.519055    0.372137    Uiso  ?  Si

Si31      1.0     0.112947    0.694570    0.386459    Uiso  ?  Si

Si32      1.0     0.101927    0.909371    0.383754    Uiso  ?  Si

Si33      1.0     0.252790    0.304722    0.317220    Uiso  ?  Si

Si34      1.0     0.253410    0.504882    0.315885    Uiso  ?  Si

Si35      1.0     0.266408    0.688791    0.319077    Uiso  ?  Si
```

```
Si36    1.0    0.262227    0.897489    0.317368    Uiso  ?  Si

Si37    1.0    0.249806    0.199672    0.251397    Uiso  ?  Si

Si38    1.0    0.246233    0.403878    0.247717    Uiso  ?  Si

Si39    1.0    0.258188    0.600175    0.240924    Uiso  ?  Si

Si40    1.0    0.258703    0.793550    0.253714    Uiso  ?  Si

Si41    1.0    0.071795    0.195568    0.202187    Uiso  ?  Si

Si42    1.0    0.075920    0.404000    0.194520    Uiso  ?  Si

Si43    1.0    0.080410    0.607955    0.194477    Uiso  ?  Si

Si44    1.0    0.084715    0.797262    0.204536    Uiso  ?  Si

Si45    1.0    0.074342    0.297951    0.131799    Uiso  ?  Si

Si46    1.0    0.083622    0.505547    0.128042    Uiso  ?  Si

Si47    1.0    0.084572    0.710365    0.124391    Uiso  ?  Si

Si48    1.0    0.079174    0.914504    0.157410    Uiso  ?  Si

Si49    1.0    0.230411    0.287244    0.066637    Uiso  ?  Si

Si50    1.0    0.229945    0.500380    0.056335    Uiso  ?  Si

Si51    1.0    0.237854    0.708914    0.055954    Uiso  ?  Si

Si52    1.0    0.230190    0.921211    0.092325    Uiso  ?  Si

Si53    1.0    0.158976    0.167793    0.034529    Uiso  ?  Si

Si54    1.0    0.193378    0.388954   -0.006243    Uiso  ?  Si

Si55    1.0    0.196936    0.606072   -0.013970    Uiso  ?  Si

Si56    1.0    0.184903    0.830656    0.015236    Uiso  ?  Si

Si57    1.0    0.368377    0.224073    0.460703    Uiso  ?  Si

Si58    1.0    0.521811    0.403229    0.406747    Uiso  ?  Si

Si59    1.0    0.522549    0.604827    0.415173    Uiso  ?  Si
```

```
Si60      1.0    0.378678    0.802127    0.459816    Uiso  ?  Si

Si61      1.0    0.830473    0.199364    0.431096    Uiso  ?  Si

Si62      1.0    0.704681    0.396415    0.444312    Uiso  ?  Si

Si63      1.0    0.704594    0.591988    0.452658    Uiso  ?  Si

Si64      1.0    0.839486    0.789414    0.429462    Uiso  ?  Si

Si65      1.0    0.420553    0.299371    0.372772    Uiso  ?  Si

Si66      1.0    0.431172    0.507321    0.364632    Uiso  ?  Si

Si67      1.0    0.418515    0.708131    0.384718    Uiso  ?  Si

Si68      1.0    0.418878    0.895609    0.383071    Uiso  ?  Si

Si69      1.0    0.742148    0.296232    0.373296    Uiso  ?  Si

Si70      1.0    0.732158    0.499503    0.373691    Uiso  ?  Si

Si71      1.0    0.728349    0.696431    0.384879    Uiso  ?  Si

Si72      1.0    0.753646    0.892695    0.380647    Uiso  ?  Si

Si73      1.0    0.582247    0.292812    0.308444    Uiso  ?  Si

Si74      1.0    0.590197    0.498413    0.299011    Uiso  ?  Si

Si75      1.0    0.579108    0.699070    0.314598    Uiso  ?  Si

Si76      1.0    0.583620    0.895503    0.323330    Uiso  ?  Si

Si77      1.0    0.911464    0.301376    0.317930    Uiso  ?  Si

Si78      1.0    0.904736    0.496486    0.321393    Uiso  ?  Si

Si79      1.0    0.915692    0.694348    0.340200    Uiso  ?  Si

Si80      1.0    0.929488    0.901069    0.328207    Uiso  ?  Si

Si81      1.0    0.577926    0.189677    0.243080    Uiso  ?  Si

Si82      1.0    0.581721    0.393423    0.236438    Uiso  ?  Si

Si83      1.0    0.585731    0.605175    0.236744    Uiso  ?  Si
```

```
Si84     1.0   0.582477   0.801785   0.246674   Uiso  ?  Si

Si85     1.0   0.908674   0.189534   0.261688   Uiso  ?  Si

Si86     1.0   0.907931   0.400879   0.247500   Uiso  ?  Si

Si87     1.0   0.914690   0.604392   0.255806   Uiso  ?  Si

Si88     1.0   0.925331   0.793406   0.265342   Uiso  ?  Si

Si89     1.0   0.408190   0.192273   0.186454   Uiso  ?  Si

Si90     1.0   0.406725   0.400565   0.184380   Uiso  ?  Si

Si91     1.0   0.418492   0.601230   0.177521   Uiso  ?  Si

Si92     1.0   0.414744   0.796983   0.188794   Uiso  ?  Si

Si93     1.0   0.752581   0.192571   0.191826   Uiso  ?  Si

Si94     1.0   0.752097   0.395696   0.180854   Uiso  ?  Si

Si95     1.0   0.760163   0.602144   0.184734   Uiso  ?  Si

Si96     1.0   0.762224   0.793995   0.200435   Uiso  ?  Si

Si97     1.0   0.403817   0.295856   0.118596   Uiso  ?  Si

Si98     1.0   0.406468   0.498095   0.107873   Uiso  ?  Si

Si99     1.0   0.412512   0.705067   0.107574   Uiso  ?  Si

Si100    1.0   0.415907   0.904523   0.125379   Uiso  ?  Si

Si101    1.0   0.759018   0.290011   0.118006   Uiso  ?  Si

Si102    1.0   0.757658   0.500694   0.115583   Uiso  ?  Si

Si103    1.0   0.763577   0.706638   0.118370   Uiso  ?  Si

Si104    1.0   0.768553   0.903906   0.142573   Uiso  ?  Si

Si105    1.0   0.583917   0.291575   0.065763   Uiso  ?  Si

Si106    1.0   0.591721   0.500288   0.055583   Uiso  ?  Si

Si107    1.0   0.599453   0.704057   0.056235   Uiso  ?  Si
```

Si108	1.0	0.603769	0.899884	0.083482	Uiso	?	Si
Si109	1.0	0.924580	0.272431	0.059420	Uiso	?	Si
Si110	1.0	0.926219	0.500112	0.059519	Uiso	?	Si
Si111	1.0	0.926002	0.721399	0.057215	Uiso	?	Si
Si112	1.0	0.934220	0.926247	0.087911	Uiso	?	Si
Si113	1.0	0.489330	0.188653	0.021998	Uiso	?	Si
Si114	1.0	0.488244	0.395451	0.024320	Uiso	?	Si
Si115	1.0	0.492046	0.604466	0.018174	Uiso	?	Si
Si116	1.0	0.495077	0.811891	0.031290	Uiso	?	Si
Si117	1.0	0.972668	0.164510	-0.006486	Uiso	?	Si
Si118	1.0	0.008037	0.385421	0.027532	Uiso	?	Si
Si119	1.0	0.011258	0.610271	0.020113	Uiso	?	Si
Si120	1.0	0.989694	0.837151	0.009529	Uiso	?	Si
C1	1.0	0.050595	0.045536	0.593377	Uiso	?	C
C2	1.0	0.150668	0.087621	0.597755	Uiso	?	C
C3	1.0	0.250444	0.045473	0.604107	Uiso	?	C
C4	1.0	0.050912	0.212640	0.590334	Uiso	?	C
C5	1.0	0.150909	0.170487	0.596089	Uiso	?	C
C6	1.0	0.051017	0.295506	0.588939	Uiso	?	C
C7	1.0	0.350408	0.087633	0.608430	Uiso	?	C
C8	1.0	0.450722	0.045425	0.609370	Uiso	?	C
C9	1.0	0.250684	0.212628	0.601967	Uiso	?	C
C10	1.0	0.350501	0.170476	0.608227	Uiso	?	C
C11	1.0	0.151271	0.337588	0.592118	Uiso	?	C

```
C12    1.0    0.250940    0.295482    0.599439    Uiso  ?  C
C13    1.0    0.051210    0.462713    0.587673    Uiso  ?  C
C14    1.0    0.151452    0.420502    0.590677    Uiso  ?  C
C15    1.0    0.051220    0.545597    0.587989    Uiso  ?  C
C16    1.0    0.550896    0.087604    0.606981    Uiso  ?  C
C17    1.0    0.650700    0.045485    0.601799    Uiso  ?  C
C18    1.0    0.450865    0.212618    0.609742    Uiso  ?  C
C19    1.0    0.551015    0.170495    0.607602    Uiso  ?  C
C20    1.0    0.350899    0.337635    0.604205    Uiso  ?  C
C21    1.0    0.451007    0.295489    0.608486    Uiso  ?  C
C22    1.0    0.251366    0.462643    0.595873    Uiso  ?  C
C23    1.0    0.351097    0.420476    0.602480    Uiso  ?  C
C24    1.0    0.151438    0.587759    0.590815    Uiso  ?  C
C25    1.0    0.251401    0.545546    0.595824    Uiso  ?  C
C26    1.0    0.051039    0.712763    0.589778    Uiso  ?  C
C27    1.0    0.151327    0.670638    0.592376    Uiso  ?  C
C28    1.0    0.050937    0.795582    0.591034    Uiso  ?  C
C29    1.0    0.750418    0.087674    0.596161    Uiso  ?  C
C30    1.0    0.850303    0.045550    0.591823    Uiso  ?  C
C31    1.0    0.650975    0.212638    0.602913    Uiso  ?  C
C32    1.0    0.750553    0.170535    0.596601    Uiso  ?  C
C33    1.0    0.551310    0.337593    0.607625    Uiso  ?  C
C34    1.0    0.651301    0.295468    0.603817    Uiso  ?  C
C35    1.0    0.451196    0.462586    0.606515    Uiso  ?  C
```

```
C36      1.0    0.551481   0.420452   0.607772   Uiso ? C

C37      1.0    0.351140   0.587620   0.602415   Uiso ? C

C38      1.0    0.451245   0.545437   0.606644   Uiso ? C

C39      1.0    0.251016   0.712667   0.599430   Uiso ? C

C40      1.0    0.351005   0.670454   0.604162   Uiso ? C

C41      1.0    0.150925   0.837669   0.596440   Uiso ? C

C42      1.0    0.250760   0.795458   0.602182   Uiso ? C

C43      1.0    0.050622   0.962665   0.593565   Uiso ? C

C44      1.0    0.150713   0.920514   0.598014   Uiso ? C

C45      1.0    0.950577   0.087705   0.590494   Uiso ? C

C46      1.0    0.850476   0.212732   0.591760   Uiso ? C

C47      1.0    0.950670   0.170533   0.589617   Uiso ? C

C48      1.0    0.751113   0.337639   0.598783   Uiso ? C

C49      1.0    0.850658   0.295575   0.592392   Uiso ? C

C50      1.0    0.651672   0.462616   0.606119   Uiso ? C

C51      1.0    0.751359   0.420536   0.600211   Uiso ? C

C52      1.0    0.551529   0.587512   0.608516   Uiso ? C

C53      1.0    0.651751   0.545379   0.606915   Uiso ? C

C54      1.0    0.451021   0.712522   0.608875   Uiso ? C

C55      1.0    0.551372   0.670393   0.608481   Uiso ? C

C56      1.0    0.350486   0.837523   0.608598   Uiso ? C

C57      1.0    0.450894   0.795359   0.610314   Uiso ? C

C58      1.0    0.250452   0.962578   0.604235   Uiso ? C

C59      1.0    0.350426   0.920378   0.608699   Uiso ? C
```

```
C60      1.0    0.950727   0.337689   0.588685   Uiso ? C
C61      1.0    0.851023   0.462714   0.594459   Uiso ? C
C62      1.0    0.950796   0.420581   0.588955   Uiso ? C
C63      1.0    0.751568   0.587572   0.601821   Uiso ? C
C64      1.0    0.851142   0.545474   0.595293   Uiso ? C
C65      1.0    0.651385   0.712581   0.605150   Uiso ? C
C66      1.0    0.751309   0.670478   0.600622   Uiso ? C
C67      1.0    0.551046   0.837524   0.608372   Uiso ? C
C68      1.0    0.651067   0.795442   0.603998   Uiso ? C
C69      1.0    0.450696   0.962572   0.609535   Uiso ? C
C70      1.0    0.550908   0.920417   0.607400   Uiso ? C
C71      1.0    0.950852   0.587699   0.589999   Uiso ? C
C72      1.0    0.850775   0.712617   0.593973   Uiso ? C
C73      1.0    0.950816   0.670589   0.590065   Uiso ? C
C74      1.0    0.750613   0.837613   0.597587   Uiso ? C
C75      1.0    0.850563   0.795469   0.592931   Uiso ? C
C76      1.0    0.650661   0.962620   0.602043   Uiso ? C
C77      1.0    0.750425   0.920493   0.596665   Uiso ? C
C78      1.0    0.950672   0.837700   0.590441   Uiso ? C
C79      1.0    0.850304   0.962674   0.592080   Uiso ? C
C80      1.0    0.950617   0.920525   0.590976   Uiso ? C
```

CIF file containing the atomic positions of the G/S SJ initial model